Simultaneous Analysis of Slope Instabilities on a Small Catchment-scale using Coupled Surface and Subsurface Flows

Yulong Zhu[a], Tatsuya Ishikawa[b*], Srikrishnan Siva Subramanian[c], and Bin Luo[d]

[a)] Yulong Zhu

Laboratory of Analytical Geomechanics, Graduate School of Engineering, Hokkaido University, Japan

e-mail: zhuyulong@eis.hokudai.ac.jp

[b*)] Tatsuya Ishikawa **(Corresponding author)**

Faculty of Engineering, Hokkaido University, Kita 13, Nishi 8, Kita-ku, Sapporo, Hokkaido 060-8628, Japan

e-mail: t-ishika@eng.hokudai.ac.jp

[c)] Srikrishnan Siva Subramanian

State Key Laboratory of Geohazard Prevention and Geo-environment Protection, Chengdu University of Technology, China

e-mail: srikrishnan@frontier.hokudai.ac.jp

[d)] Bin Luo

Department of Road and Bridge Engineering, School of Civil Engineering, Sichuan Agricultural University, China

e-mail: bin-luo@sicau.edu.cn

Highlights

1. A coupled model of surface flow, subsurface flow, and soil mechanics is proposed.
2. Slope instabilities are analyzed on a small catchment-scale.
3. Runoff increases the possibility of embankment collapse at the exit of the gully.

Abstract

High-velocity runoff generated in hillslopes during heavy rainfall caused by typhoon increases the instability of the embankment slope at the exit of the gully. Such effects of high-velocity runoff are usually neglected in conventional rainfall-induced slope failure analysis. In order to consider the effects of runoff on the slope instability, this study attempts to simulate the runoff, infiltration, seepage, and slope instabilities on a small catchment-scale simultaneously. For this purpose, this study firstly proposes a coupled model of surface flow, subsurface flow, and soil mechanics based on shallow water equations, Richards's equation, Green-Ampt infiltration capacity model, and local factor of safety (LFS) approach. Next, to make the proposed coupled model effective in the practical analysis of runoff, a diffusion wave approximation of shallow water equations is validated by numerical simulations, and then it is used to replace shallow water equations in the proposed coupled model. Finally, the proposed coupled model is verified by Abdul and Gillham system and applied to a natural slope in Hokkaido, Japan. The numerical results highlight the influences of runoff from upstream on the embankment slope failure at the exit of the gully. Furthermore, the small catchment-scale slope instabilities assessment approach proposed in this study provides an effective approach for simulating heavy rainfall induced runoff and slope instabilities. The distribution map of the factor of safety (FOS) has significant implications for precisely determining the dangerous spots (instead of areas) on a small catchment-scale and accurately releasing the warning information to these dangerous spots.

Keywords: Surface flow; Subsurface flow; Slope instabilities; Local factor of safety

1 Introduction

The rainstorms and unexpected typhoons cause sediment-related disasters threatening the lives and public property in many parts of the world, especially in rainy mountainous

terrains. During a rainstorm, the infiltration capacity of the slope is not enough to absorb all the rainwater into the soil, resulting in the rainwater that cannot infiltrate into the soil flows in the form of runoff on the slope surface (Cuomo and Della Sala, 2013; Kean et al., 2013; Wei et al., 2017; Van Asch et al., 2018). Both rainwater infiltration and runoff could deteriorate the slope stability. The rainwater infiltration causes a decrease in the suction in the unsaturated zone and an increase in positive pore pressure in the saturated zone due to groundwater, which eventually induces the occurrence of landslide/slope failure (Chowdhury and Flentje, 2002; Rahardjo et al., 2005; Acharya et al., 2009; Zhang et al., 2014). On the other hand, the runoff, i.e. fast-flowing surface water, may cause erosion of the slope surface or pond in the concave areas increasing the possibility of slope failure at some locations such as a road embankment which crosses a gully. For example, during the summer season (August-September), the Japanese archipelago is often struck by violent typhoons with extremely intense rainfalls, which cause a large number of disasters, e.g. floods, debris flows, and landslides (Wang and Sassa, 2003; Fujisawa et al., 2010). According to the statistics of the Ministry of Land, Infrastructure, Transport, and Tourism (MLIT), there are 200,000 dangerous valleys and slopes in Japan, and about 1,000 landslide disasters reported annually (Osanai et al., 2010).

Both on catchment-scale and slope-scale, when analyzing the unsaturated soil slope instability under rainwater infiltration, for simplification, the influences of runoff are usually neglected (Liu et al., 2017; Chiu et al., 2019). In this case, two assumptions of the rainfall infiltration are generally used. One is that the rainfall infiltration is equal to the rainfall intensity. Another is that rainfall infiltration is equal to the component of rainfall intensity perpendicular to the boundary. Obviously, the above assumptions cannot fully reproduce the actual processes of rainfall/runoff infiltration, especially under heavy rainfall conditions (rainfall intensity is much larger than the infiltration capacity). Therefore, earlier studies made many attempts to

develop models that can describe the behavior of surface and subsurface flows. Tian and Liu (2011) coupled two-dimensional (2D) Saint Venant equations and three-dimensional (3D) Richards's equation in an Integrated Surface Water-Ground water Model (ISWGM). Fernández-Pato et al. (2016) combined 2D shallow water equations with two infiltration models, Horton model and Green-Ampt model, for estimating the runoff and infiltration in a watershed. However, there are no simplified methods or numerical models developed to simulate the slope instability by coupled surface and subsurface flows during heavy rainfall.

From the view of slope stability analysis, the limit-equilibrium method (LEM) and shear strength reduction technique (SSRT) are commonly used in some general commercial software packages e.g. GeoStudio (GEO-SLOPE International, 2007) and FLAC^{3D} (Itasca, 2012). The LEM discretizes the mass of a potential failure slope into smaller vertical slices and assesses the ratio of shear strength to shear stress for all slices as the factor of safety (FOS) of an identified or assumed potential failure surface (Bishop, 1955; Morgenstern and Price, 1965). While the determination of where the failure initiates or the ultimate geometry and position of a landslide failure surface is one of the fundamental challenges when using LEM (Lu et al., 2012). Unlike conventional LEM, it is not necessary to specify the shape of the failure surface in advance when using the SSRT (Sciarra et al., 2017; Pasculli et al., 2018). The FOS is defined as the ratio of the real shear strength to the reduced shear strength of the soil. The failure surface is determined by reducing the shear strength parameters (cohesion and friction angle) of the soil until the slope becomes unstable (Farshidfar and Nayeri, 2015). However, it is worth noting that LEM and SSRT are effective for the stability analysis of a single slope but not feasible for the analysis of slope instabilities on a catchment-scale. Lu et al. (2012) proposed an approach, i.e. local factor of safety (LFS) approach to quantify the FOS of a slope under rainwater infiltration, and verified that the assessment of the LFS approach is consistent with the LEM.

105 Furthermore, the LFS approach has the potential to overcome several major limitations in the
106 classical FOS methodologies, such as the initiation and evolution of instability with changes in
107 pore water pressure, and the inherent underestimation of slope instability (Lu et al., 2012).
108 Besides, when analyzing the stability of multi slopes (more than one slope), LEM and SSRT
109 need to analyze the slopes one by one. However, the LFS approach also has the potential to
110 give the distribution map of FOS. Therefore, in this study, the LFS approach is used to assess
111 the slope instabilities on a small catchment-scale.

112 Accordingly, the objectives of this study are to (1) develop a coupled model of surface
113 flow and subsurface flow to simulate the relationship between rainfall, runoff, and infiltration
114 under heavy rainfall conditions; (2) model the rainfall/runoff induced slope instabilities to
115 determine the dangerous spots on a small catchment-scale. For these purposes, this study firstly
116 proposes a coupled model of surface flow, subsurface flow, and soil mechanics to
117 simultaneously simulate runoff, infiltration, seepage, and slope instabilities on a small
118 catchment-scale. Surface flow is governed by 2D shallow water equations. Subsurface flow is
119 governed by 3D Richards's equation. Two well-known models, namely Horton model (Horton,
120 1933) and Green-Ampt model (Green and Ampt, 1911), are commonly used to estimate soil
121 infiltration capacity. The parameters in the Horton model have no clear physical basis and must
122 be estimated from the experimental data, while the parameters in the Green-Ampt model have
123 physical meaning and can be estimated from soil properties (Fernández-Pato et al., 2016).
124 Therefore, the Green-Ampt model is used in this study for estimating the infiltration capacity
125 of the ground surface, which could be used to determine the boundary conditions of subsurface
126 flow analysis. The LFS approach is used to assess the slope instabilities on a small catchment-
127 scale. Next, to make the proposed coupled model effective in the practical analysis of runoff,
128 a diffusion wave approximation of shallow water equations is validated based on numerical

129 simulations. Afterward, the diffusion wave approximation is used to replace shallow water
130 equations in the proposed coupled model. Then, the proposed coupled model is verified by
131 Abdul and Gillham system (Abdul and Gillham, 1984). Finally, the simulation of surface flow,
132 subsurface flow, and slope instabilities for a natural mountain area in Hokkaido, Japan is
133 performed by using the proposed coupled model.

134 **2 Numerical Modeling Strategy**

135 The surface and subsurface flows are complex environmental systems that often behave
136 in a coupled manner. In this study, a coupled model of surface flow, subsurface flow, and soil
137 mechanics is proposed by using a finite element software, COMSOL Multiphysics (COMSOL
138 Multiphysics, 2018). In the coupled model, the 3D soil mechanics model (linear elastic model)
139 is established by the solid mechanics module of COMSOL. The 2D surface flow model
140 (shallow water equations) and 3D subsurface flow model (Richards's equations) are established
141 by the PDEs (partial differential equations) module of COMSOL. The surface flow model and
142 subsurface flow model are coupled through infiltration and exfiltration. The subsurface flow
143 model and soil mechanics model are coupled in two ways: (1) the body load function that
144 depends on the volumetric water content is applied to a linear elastic soil mechanics model to
145 manifest the effect of moisture variation on the self-weight and stress distribution, and (2) the
146 effect of volumetric water content variation on the pore water pressure (suction) is considered
147 for evaluating effective stress. Accordingly, the local factor of safety can be calculated by using
148 effective stress as shown in Fig. 1.

149 During torrential rain, rainwater infiltration is a two-stage process, i.e. rainfall
150 infiltration (rainfall derived infiltration) in the early stage of the rainfall event, and runoff
151 infiltration (runoff derived infiltration, in this case, the infiltration is controlled by the pressure
152 gradient rather than the rainfall intensity) in the later stage of the rainfall event. Therefore, the

Green-Ampt model is used for estimating the infiltration capacity (f_p) of the ground surface to determine the boundary conditions of subsurface flow analysis. That is in the early stage of the rainfall event, as the rainfall intensity (R) is usually weak and less than the infiltration capacity (f_p) of the ground surface, the Richards's equation is directly solved with a flux boundary condition at the surface. If the rainfall intensity exceeds the infiltration capacity (f_p), part of rainwater infiltrates into the ground, and the rest generates runoff on the ground surface. On the other hand, the exfiltration (positive value) and infiltration (negative value) calculated from the subsurface flow model is added to the surface flow model as a source and sink item. Then, the infiltrated rainwater causes the decrease of the infiltration capacity (f_p) of the ground surface, and the calculation of the next timestep will be carried out. This study proposes an iterative cross-coupled surface and subsurface flows model to simulate this process. The flowchart of the time-marching scheme in iterative cross-coupled surface and subsurface flows model is shown in Fig. 2.

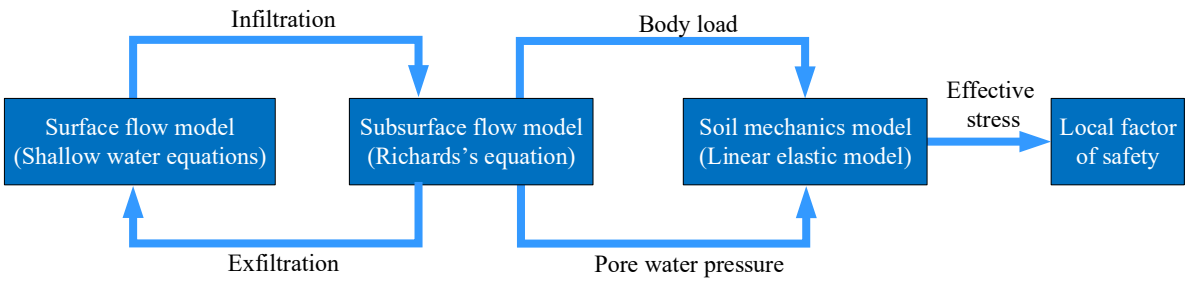

Fig. 1. Scheme of the proposed coupled hydrological and slope stability model.

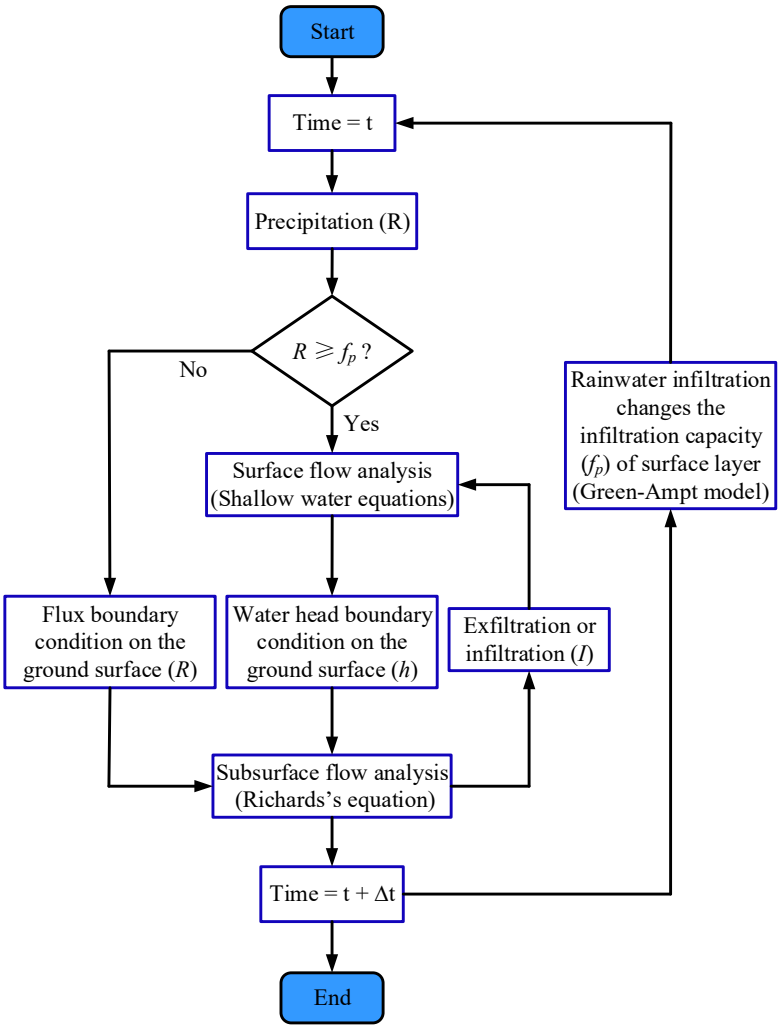

Fig. 2. Flowchart of the time-marching scheme in iterative cross-coupled surface and subsurface flows model.

3 Governing Equations

The governing equations in the proposed coupled model are represented in this part. The surface flow is governed by the 2D shallow water equations, and the subsurface flow is governed by the 3D Richards's equation. The soil infiltration capacity is estimated by the Green-Ampt model, and the slope instabilities are assessed by the LFS approach.

3.1 Governing equation for surface flow

Surface flow is calculated by 2D shallow water equations which can be expressed as follows (Murillo et al., 2007).

Equation of continuity:

$$\frac{\partial h}{\partial t} + \frac{\partial (hu)}{\partial x} + \frac{\partial (hv)}{\partial y} = R - I \tag{1}$$

Equations of motion:

$$\frac{\partial (uh)}{\partial t} + \frac{\partial (hu^2)}{\partial x} + \frac{\partial (huv)}{\partial y} = -hg\frac{\partial H}{\partial x} - hgS_{fx} + D_x \tag{2}$$

$$\frac{\partial (vh)}{\partial t} + \frac{\partial (huv)}{\partial x} + \frac{\partial (hv^2)}{\partial y} = -hg\frac{\partial H}{\partial y} - hgS_{fy} + D_y \tag{3}$$

where, h is water depth (m); u, v is water velocity in the x and y direction (m/s); R is rainfall intensity (m/s); I is infiltration rate (m/s); g is the gravitational acceleration (m/s^2); H is water surface elevation (m); t is time (s); D_x, D_y is advection term in the x and y direction; S_{fx}, S_{fy} is the friction slope in the x and y direction respectively, usually written in term of the Manning's roughness coefficient n_m (s/m$^{1/3}$).

$$S_{fx} = n_m^2 u\sqrt{u^2 + v^2}/h^{4/3}\ , S_{fy} = n_m^2 v\sqrt{u^2 + v^2}/h^{4/3} \tag{4}$$

The first terms on the right-hand side of the equations of motion, Eq. (2) and Eq. (3), represent the driving forces from the slope gradient and water depth gradient. The second terms represent the drag forces due to friction (friction loss gradient). The third terms are advection terms, and they can be assumed by the following conditions.

$$D_x = \frac{\partial}{\partial x}\left[v_t \frac{\partial (uh)}{\partial x}\right] + \frac{\partial}{\partial y}\left[v_t \frac{\partial (uh)}{\partial y}\right] \quad , \quad D_y = \frac{\partial}{\partial x}\left[v_t \frac{\partial (vh)}{\partial x}\right] + \frac{\partial}{\partial y}\left[v_t \frac{\partial (vh)}{\partial y}\right] \tag{5}$$

In which, v_t is eddy viscosity coefficient (m^2/s), and it can be assumed as follows (Zeng et al., 2010).

$$v_t = \lambda h U^* \text{ and } U^* = \sqrt{ghS} \quad (6)$$

where, U^* is the frictional velocity (m/s); λ is dimensionless eddy viscosity, and its standard value for an infinitely wide channel is 0.067 (Zeng et al., 2010); S is the gradient of water surface. As the water depth gradient is much smaller than the slope gradient, it can be assumed that S is equal to the slope gradient (Weill et al., 2009) as shown in Fig. 3.

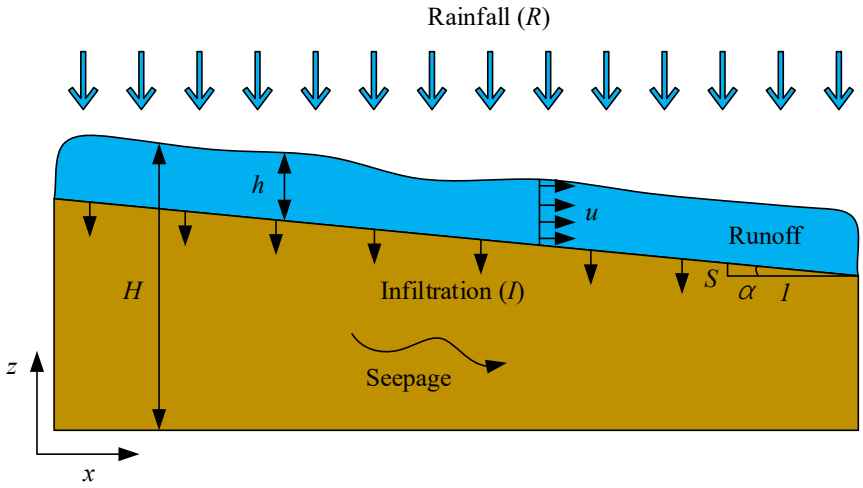

Fig. 3. Conceptual schematic of the surface flow model.

In principle, by simultaneously solving the equations of continuity and motion, the behavior of the surface runoff can be tracked, and the water depth and velocity can be obtained at any interesting location. However, the timesteps need to be set very small, or simulations only can be performed under relatively flat terrain conditions. It causes the low calculation efficiency of shallow water equations when performing the practical runoff analysis in vast mountainous areas (Rengers et al., 2016). The main reason can be considered as that some insignificant terms in the equation of motion, Eq. (2) and Eq. (3), significantly increase the calculation time and decrease convergence. Therefore, to ignore the insignificant terms in the equations of motion, the contribution of each term is examined by performing numerical simulations using seven surface flow models with different slope angles (<1˚, 5˚, 10˚, 15˚, 30˚,

45˚, and 60˚). In the surface flow model, Manning's coefficient value is 0.3 s/m$^{1/3}$. A fixed water head boundary condition (h=0.001 m) is applied to the left side and zero gradient boundary condition ($\partial h/\partial x$=0) is applied on the right side. The simulation time is 10 s with the timestep of 1.0 ×10^{-4} s. Table 1 shows the simulation results, i.e. the contribution of each term in Eq. (2) as a fraction of 100 % of the total for surface water flow under different slope angles.

Table 1 Contribution of each term in the equations of motion for surface water flow.

Slope angle (˚)	Inertia term $\frac{\partial(uh)}{\partial t}$ (%)	Velocity term $\frac{\partial(hu^2)}{\partial x}$ (%)	Driving force term $-hg\frac{\partial H}{\partial x}$ (%)	Friction term $-hgS_{fx}$(%)	Advection term D_x(%)
<1	<0.001	<0.001	50.038	49.961	<0.001
5	<0.001	0.005	49.584	50.410	<0.001
10	<0.001	0.011	49.595	50.393	<0.001
15	0.003	0.015	49.535	50.446	0.001
30	0.024	0.219	52.537	47.200	0.020
45	0.051	0.850	44.260	54.730	0.109
60	0.159	0.327	50.808	48.679	0.027

From the results, it is clear that the sum of the driving force term and friction term accounts for over 99% for all types, while the total contribution of the inertia term, advection term, and velocity term is less than 1% together. Therefore, the following diffusion wave approximation can be typically used in practice.

$$S_{fx} + \frac{\partial H}{\partial x} = 0 \tag{7}$$

$$S_{fy} + \frac{\partial H}{\partial y} = 0 \tag{8}$$

After substituting Eq. (4) into Eq. (7) and Eq. (8), the expressions for the components of the velocity vector can be obtained as follows.

$$u = -\frac{h^{2/3}}{n_m\sqrt{|S|}}\nabla_x(H)\ ,\quad v = -\frac{h^{2/3}}{n_m\sqrt{|S|}}\nabla_y(H) \tag{9}$$

Finally, Eq. (1) can be written as follows, and then it is used to replace shallow water equations in the proposed coupled model.

$$\frac{\partial h}{\partial t} - \nabla\left(\frac{h^{5/3}}{n_m\sqrt{|S|}}\nabla(H)\right) = R - I \tag{10}$$

3.2 Governing equation for subsurface flow

When performing subsurface flow analysis in unsaturated soils, two well-known methods are commonly used: Richards's equations and two-phase Darcy's law method. Compared with the two-phase Darcy's law method, Richards's equation is simple in form and the physical meaning of each parameter is relatively clear. Therefore, the subsurface flow is governed by 3D Richards's equation (Richards, 1931).

$$\nabla\cdot\left[k_s\, k_r\cdot\nabla\left(H_p + z\right)\right] + Q_w = \left[C_m + S_e S_c\right]\frac{\partial H_p}{\partial t} \tag{11}$$

where, C_m is specific moisture capacity (m^{-1}); S_c is specific storage coefficient (m^{-1}); S_e is the effective degree of saturation; H_p is pressure head (H_p is negative in unsaturated soil, and positive in saturated soil) (m); z is elevation (m); k_r is relative hydraulic conductivity; k_s is saturated hydraulic conductivity (m/s); Q_w is sink and source of water (s^{-1}).

van Genuchten (1980) proposed a Soil Water Characteristic Curve (SWCC) to describe the relationship in C_m, S_e, k_r, θ, and H_p in unsaturated soil. As shown in Eq. (12) to Eq. (15), these parameters could be specified by the saturated and residual volumetric water content θ_s and θ_r, as well as constants of a, n, m, and l.

$$\theta = \theta_r + S_e(\theta_s - \theta_r) \tag{12}$$

$$S_e = \frac{1}{\left[1+(aH_p)^n\right]^m}\quad ,\quad m = 1 - \frac{1}{n} \tag{13}$$

$$C_m = \frac{am}{1-m}(\theta_s - \theta_r)S_e^{\frac{1}{m}}(1 - S_e^{\frac{1}{m}})^m \quad (14)$$

$$k_r = S_e^{\,l}\left[1 - (1 - S_e^{\frac{1}{m}})^m\right]^2 \quad (15)$$

3.3 Soil infiltration capacity model

The Green-Ampt model (Green and Ampt, 1911) assumes that the soil infiltration capacity is governed by the soil properties and rainfall conditions. The soil infiltration capacity, f_p, can be approximated as follows.

$$f_p = k_s\left(1 + \frac{\Psi\Delta\theta}{F}\right) \quad (16)$$

where, f_p is infiltration capacity (m/s); ψ is the average suction head at the wetting front (m), and $\Delta\theta$ is the difference between the saturated volumetric water content, θ_s, and the initial volumetric water content, θ_i, ($\Delta\theta$=θ_s-θ_i) (m^3/m^3). F is the cumulative infiltration (m).

$$F = \int_0^t I dt \quad (17)$$

In this study, it is considered that the Green-Ampt model is only used to estimate the infiltration capacity (f_p) during the rainfall infiltration stage and determine when the runoff generate. At the beginning of the simulation, a profile with initial moisture content is used to determine the initial infiltration capacity of the ground surface. With infiltration of the rainwater, the Green-Ampt model is running and infiltration capacity will be redistributed at each timestep according to Eq. 16. Afterward, the rainfall intensity at the next timestep will be compared with the updated infiltration capacity. If the rainfall intensity exceeds the infiltration capacity of the ground surface, the water is ponding on the ground surface. The infiltration rate will be determined by pressure head at the surface (zero or higher depending on the increasing runoff h) and the pressure head in the cell below. A part of the not infiltrated water and the exfiltrated water from the underground will then be applied to the runoff simulation as source item in the next timestep.

3.4 3D soil mechanics model (LFS approach)

Lu et al. (2012) proposed the LFS approach to quantify the factor of safety (FOS) of a point based on the current state of stress and the change in the suction (u_a-u_w) caused by rainwater infiltration. The pore water pressure, u_w, can be calculated by the pressure head, H_p, ($u_w=\rho_w g H_p$, ρ_w is the density of water with the value of 1000 kg/m^3). Afterward, the 3D distribution of soil moisture and related u_w in the saturated and unsaturated zone during a rainfall event is coupled with the 3D soil mechanics model in two ways. One is that the volumetric water content, θ, is applied to the 3D soil mechanics model as body load to manifest the effect of moisture variation on the self-weight and stress distribution as follows.

$$\nabla \cdot (\boldsymbol{\sigma}) + \gamma(\theta)\mathbf{b} = 0 \tag{18}$$

where, $\boldsymbol{\sigma}$ is the stress tensor (kPa); $\mathbf{b}$ is the unit vector of body forces, and γ is the bulk unit weight (N/m^3), which is a function of the volumetric water content θ.

Another is that the negative pore water pressure (suction) in the unsaturated zone will increase the effective stress of the soil, while the positive pore water pressure in the saturated zone due to groundwater will decrease the effective stress of the soil. The influence of the suction on the effective stress is evaluated with Bishop's effective stress (Bishop, 1954).

$$\sigma' = (\sigma - u_a) + \chi(u_a - u_w)\,,\ \chi = \frac{S_e - S_r}{1 - S_r} \tag{19}$$

where, σ' is effective stress (kPa); u_a is the pore air pressure (kPa); u_w is the pore water pressure (kPa), and χ is the matrix suction coefficient which varies from 0 to 1 depending on the degree of saturation. S_r is the residual degree of saturation. Finally, the local factor of safety (F_{LFS}) at each point within a hillslope can be defined as follows.

$$F_{LFS} = \frac{2\cdot\cos\phi'}{\sigma_1' - \sigma_3'}\left[c' + \frac{\sigma_1' + \sigma_3'}{2}\tan\phi'\right] \tag{20}$$

where, c' is the effective cohesion (kPa); ϕ' is the effective friction angle (°); σ_1' and σ_3' are the maximum and minimum principal stress for the unsaturated soil (kPa).

4 Validation of the Iterative Cross-coupled Surface and Subsurface Flows Model

In this part, the iterative cross-coupled surface and subsurface flows model proposed in chapter 2 is verified by the experimental system presented by Abdul and Gillham (1984). The experimental system is composed of a 1.4 m×1.2 m×0.08 m Plexiglas box filled with medium-fine sand as illustrated in Fig. 4(a). The free water is drained off at the toe of the slope, and the initial water table is located at the toe of the slope. The soil properties are shown in Fig. 4(a). A rainfall rate of 43.2 mm/hr is applied on the whole surface domain in the first 20 minutes of a total time of 25 minutes. To verify the simulation results of the proposed coupled model, the experimental system is also simulated by a commercial software, GETFLOWS (GETFLOWS, 2014), which is a finite difference fluid flow numerical simulator. Kitamura et al. (2016) and Malow et al. (2017) validated the applicability of GETFLOWS for simulating the surface flow and subsurface flow process by comparing the simulation results of GETFLOWS and measurements of river water levels in the area of eastern Fukushima Prefecture in Japan and the area of Kourtimalei in Djibouti, respectively. The difference between GETFLOWS and the proposed model in this study in terms of theory and governing equations is that GETFLOWS simulate surface and subsurface flows in a fully coupled way by using air and water two-phase flows, and the governing equation of mass conservation is expressed as follows (Mori et al., 2015).

$$\frac{\partial(\varphi S_p)}{\partial t} - \nabla \cdot (u_p) = q_p \ , \ p = (\text{water}, \text{air}) \tag{21}$$

where, subscript p indicates fluid phase, water (w) or air (a); φ is the effective porosity (m^3/m^3); S_p is fluid saturation of p phase, ($S_w + S_a = 1$); u_p is the fluid flow velocity of p phase (Pa); q_p is the volumetric flux of sink and source of p phase ($m^3/m^3/s$).

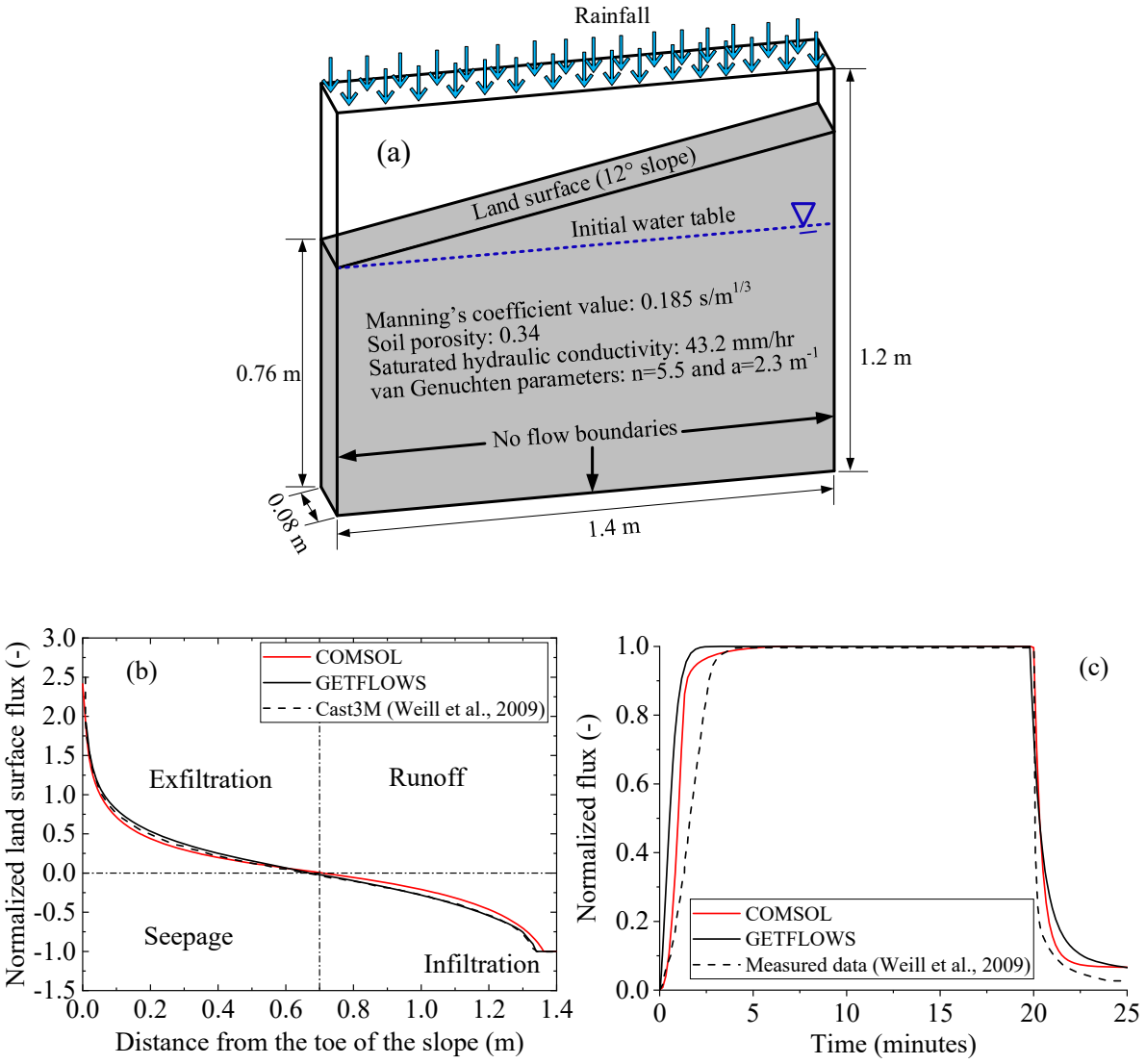

Fig. 4. (a) Abdul and Gillham system; (b) Comparison of calculated results of normalized flux along the land surface at the 19 minutes after rain; (c) Comparison of calculated results and measured data of normalized flux of discharge at the toe of the slope.

Fig. 4(b) and Fig. 4(c) plot the results calculated by COMSOL and GETFLOWS compared with the results calculated by Cast3M (a finite element code that was used by Weill et al. (2009) for modeling surface/subsurface flow in a fully integrated way, which is similar to GETFLOWS), and measured data referred from Weill et al. (2009). Fig. 4(b) shows the fluxes along the land surface, and all the fluxes are normalized by the rainfall flux imposed at the land surface (entering fluxes are negative by convention). The results imply that the models

implemented in COMSOL and GETFLOWS are able to describe the three surface regimes (infiltration, runoff, and exfiltration) along the land surface: in a small area at the top of the slope, all rainwater infiltrates into the soil (normalized flux equals -1); in the upper half of the slope, part of the rainwater infiltrates, and the rest flows in the form of runoff on the land surface (normalized flux between -1 and 0); at the lower half of the slope, groundwater exfiltrates to the land surface and flows out with the runoff from the upper part (normalized flux positive). Fig. 4(c) displays the normalized flux of discharge at the toe of the slope calculated by COMSOL and GETFLOWS compared with the data measured by Weill et al. (2009). It shows that the calculated results agree well with the measured data, though the simulated time to reach the steady state of overland water and groundwater exchange is shorter than the experimental one. The presence of air could significantly slow down the infiltration process (Weill et al., 2009), and the inconsideration of this effect in the modeling approach could be responsible for that.

5 Case Study of Typhoon Induced Embankment Slope Failures

5.1 Outline of disasters

In 2016, from the Pacific, Typhoon No.10 (Lionrock) landed on Hokkaido, Japan on August 29th-31st, and the sediments eroded and transported from slopes and banks during the event were estimated to be approximately 3.7×10^5 m^3 within the Pekerebetsu catchment in Hokkaido, Japan (Furuichi et al., 2018). Near to Nissho Pass along the National Highway Route 274 in Hokkaido, Japan, Typhoon No.10 triggered intense landslides, embankment collapses, and debris flows as shown in Fig. 5(a). According to the rainfall records obtained from Automated Meteorological Data Acquisition System (AMeDAS), the observed cumulative rainfall that fell from 19:00 on August 28th to 10:00 on August 31st was 488 mm with the peak value of 55 mm at 01:00 on August 31st as shown in Fig. 5(b), which is the highest rainfall ever

recorded in that area. Based on the prediction of the occurrence of sediment-related disasters by the Japanese early warning system, the road was closed from 11:15 on August 30th, and Hokkaido government released heavy rainfall warning information, flood warning information, and disaster warning information at 17:00, 19:00, and 22:00 on August 30th, respectively.

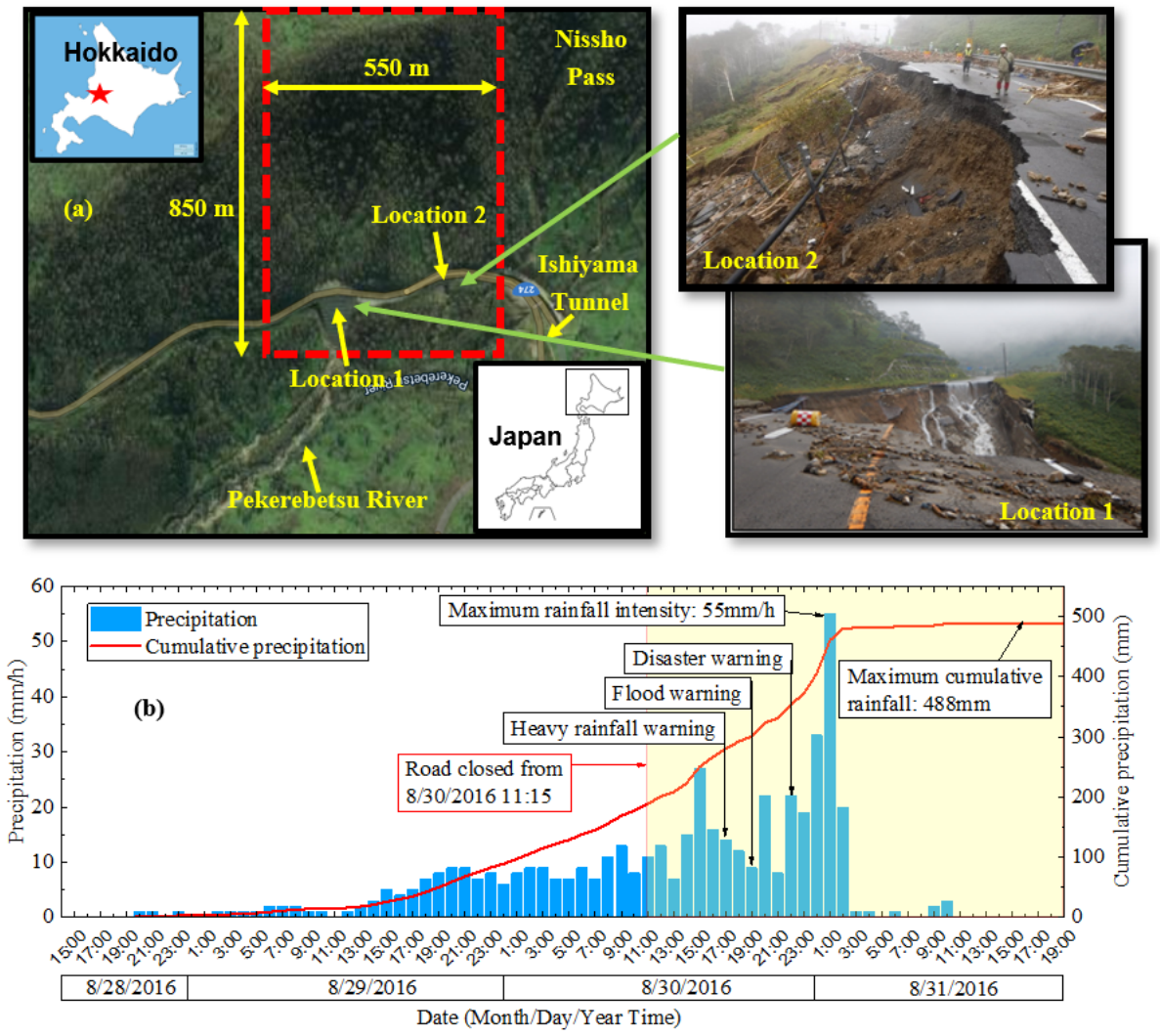

Fig. 5. (a) Locations of slope failures induced by Typhoon No.10 along National Highway Route 274; (b) Rainfall recorded during Typhoon No.10 at Nissho Pass.

5.2 Simulation of surface and subsurface flows for a natural mountain area

The surface flow and subsurface flow analysis at Nissho Pass are performed by the proposed coupled model. Based on the digital elevation model (DEM) produced from airborne

laser scanning (1m resolution), a 3D model for a natural mountain area (surrounded by the red dashed box in Fig. 5(a)) for slope instabilities assessment with surface and subsurface flows analysis is built as shown in Fig. 6. The model is composed of three parts: weathered granite, soil, and embankment. Soil properties are listed in Table 2. The parameters, i.e. dry density (ρ_s), saturated hydraulic conductivity (k_s), saturated volumetric water content (θ_s), effective cohesion (c'), and effective friction angle (ϕ'), have been obtained from laboratory element tests (Sato et al., 2017). The parameters for which no results of laboratory tests are available, i.e. residual volumetric water content (θ_r) and van Genuchten parameters (α and m), were estimated based on the grain size curve of soil (SoilVision, 2018). Although there were three other typhoons before Typhoon No.10, since they were at least one week apart from Typhoon No.10, they had little effect on the groundwater level during Typhoon No.10. Therefore, the initial groundwater level is set to -5.5m from the ground surface according to the historical measured average value in the same period of previous years. Manning's coefficient value is 0.3 s/m$^{1/3}$ for the slope, which is the recommended value of Japan Institute of Country-ology and Engineering (JICE) for mountain grassland. The simulation time is from 19:00 on August 28th, 2016 to 17:00 on August 31st, 2016 for a total of 70 hours with the timestep of 1 hour.

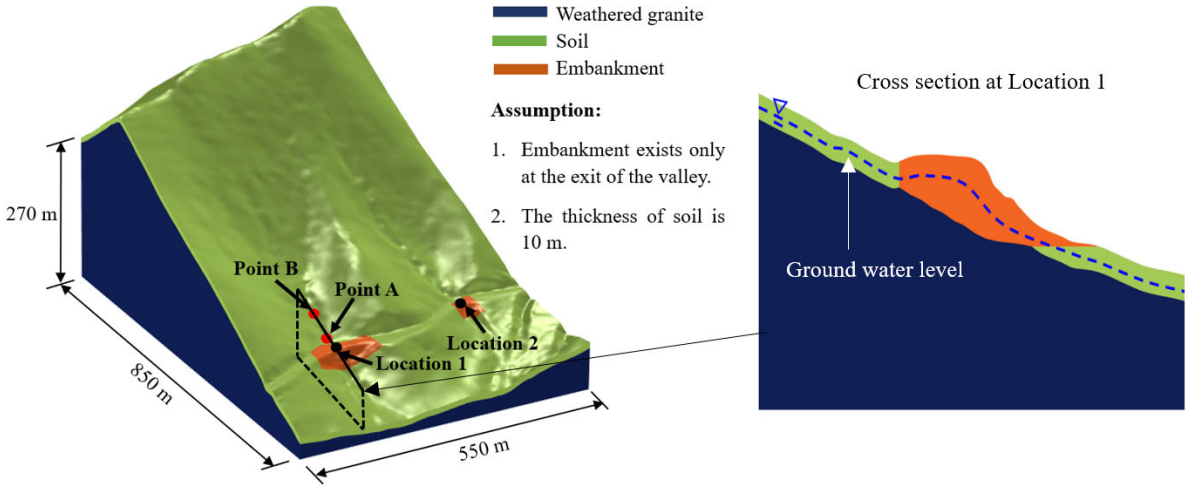

Fig. 6. Three-dimensional numerical model of a natural mountain area at Nissho Pass.

Table 2 Soil properties used for the simulation of the natural mountain area.

Parameters	Embankment	Soil	Weathered granite
Dry density, ρ_s (kg/m^3)	1695	1020	2000
Effective cohesion, c' (kPa)	0	0	37
Effective friction angle, ϕ' (°)	37	35	21
Saturated hydraulic conductivity, k_s (m/s)	1.12×10^{-5}	1.4×10^{-6}	3.47×10^{-9}
Saturated volumetric water content, θ_s (m^3/m^3)	0.36	0.63	0.48
Residual volumetric water content, θ_r (m^3/m^3)	0.035	0.19	0.008
van Genuchten parameter, α (1/m)	0.538	0.810	0.012
van Genuchten parameter, m	0.468	0.437	0.246

As there are no measurement data at the locations where the slope failures occurred, the simulated results in this study are theoretically verified by a physical runoff model (Tank model) proposed by Sugawara et al. (1974), which uses multi-layered tanks to simulate rainwater infiltration and surface runoff. The Tank model has been proved that it is effective for describing the outflow in the watershed (Hong et al., 2015). The calculation of runoff is based on the generic value of the parameters suggested by Okada (2001) as listed in Fig. 7. The water storage depth (mm) for each tank is calculated based on the equations below.

$$\frac{dH_1}{dt} = R - I_1 - q_{11} - q_{12} \tag{22}$$

$$\frac{dH_2}{dt} = I_1 - q_2 - I_2 \tag{23}$$

$$\frac{dH_3}{dt} = I_2 - q_3 - I_3 \tag{24}$$

The outflow rate from each outlet of the model and infiltration rate from the upper tank to the lower tank is calculated based on the equations below.

$$q_{11} = \begin{cases} \alpha_{11} \times (H_1 - L_{11}) & , \text{if } H_1 > L_{11} \\ 0 & , \text{if } H_1 \le L_{11} \end{cases} \tag{25}$$

$$q_{12} = \begin{cases} \alpha_{12} \times (H_1 - L_{12}) & , \text{if } H_1 > L_{12} \\ 0 & , \text{if } H_1 \le L_{12} \end{cases} \quad (26)$$

$$q_2 = \begin{cases} \alpha_2 \times (H_2 - L_2) & , \text{if } H_2 > L_2 \\ 0 & , \text{if } H_2 \le L_2 \end{cases} \quad (27)$$

$$q_3 = \begin{cases} \alpha_3 \times (H_3 - L_3) & , \text{if } H_3 > L_3 \\ 0 & , \text{if } H_3 \le L_3 \end{cases} \quad (28)$$

$$I_1 = \beta_1 \times H_1,\ I_2 = \beta_2 \times H_2,\ I_3 = \beta_3 \times H_3 \quad (29)$$

The total outflow rate of the basin is represented as follows.

$$Q = (q_{11} + q_{12} + q_2 + q_3) \times A \quad (30)$$

where, I_1, I_2, and I_3 are the infiltration rate from the upper tank to the lower tank (mm/h); q_{11}, q_{12}, q_2, and q_3 are the outflow rate (mm/h) for each outlet of sidewall; L_{11}, L_{12}, L_2, and L_3 represent each outlet height (mm); H_1, H_2, and H_3 are the water storage depth (mm) in each layer; α_{11}, α_{12}, α_2, and α_3 are the outflow coefficient (1/h) for each outlet; β_1, β_2, and β_3 are the coefficients of permeability (1/h) from the bottom hole of each tank; Q is total of outflow rate of the basin (m^3/s), and A is the area of the basin (km^2).

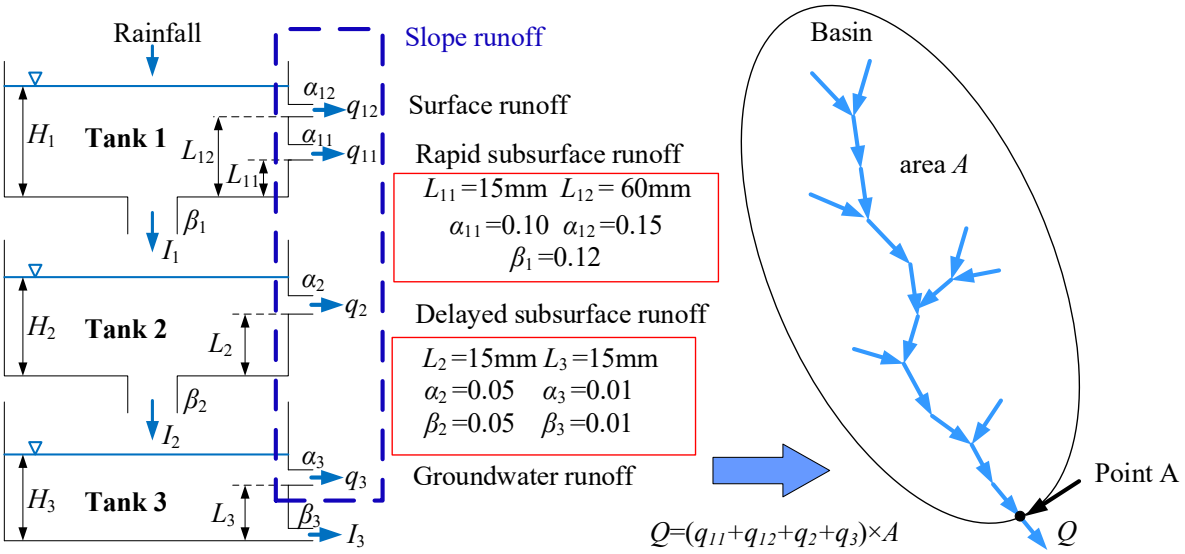

Fig. 7. Schematic diagram of the three-layer Tank model.

Fig. 8(a) displays the distribution of water depth and the vector of flow velocity calculated by COMSOL. From Fig. 8(a), it can be seen that a large amount of water from the upstream is gathered at Location 1 and Location 2, which allows more water to infiltrate into the embankment. The outflow rates of the catchment area at Location 1 (Point A in Fig. 6 and Fig. 7) calculated by the Tank model, COMSOL, and GETFLOWS are shown in Fig. 8(b). To avoid the calculation errors caused by the water coming from Location 2 along the road (see Fig. 5(a) and Fig. 8(a)), Point A is located on the edge of the embankment on the side of the mountain. From Fig. 8(b), it is recognized that the outflow rates calculated by the Tank model, COMSOL, and GETFLOWS are quite similar suggesting that the numerical results are reliable. Tank model assumes that the slope runoff flows out of the catchment area according to a certain percentage of water storage depth in each tank. Accordingly, the Tank model does not consider the impact of slope angle, which causes the outflow rate calculated by the Tank model is smaller at the peak value, and larger at the end of the rainfall event than that calculated by COMSOL and GETFLOWS. Fig. 8(c) plots the surface water depth located at the road center (where water comes from the upstream catchment and road) at Location 1 and Location 2. To discuss the two-stage process of rainwater infiltration, a representative point on the hillside slope (Point B in Fig. 6, located in the gully upstream of Location 1) is selected to display the relationship between infiltration rate and rainfall intensity on the hillside slope as shown in Fig. 8(d). The results shown in Fig. 8(d) suggest that at the beginning of a rainfall event, the infiltration rate is equal to the rainfall intensity (all rainwater infiltrates into the soil). From Fig. 8(c), it is recognized that the runoff simulated by COMSOL and GETFLOWS is generated from 22 hours after the rainfall event happens, which is consistent with the results calculated by the Tank model shown in Fig. 8(b). Nearly at the same time, rainfall intensity exceeds the infiltration capacity (f_p) of the ground surface in Fig. 8(d).

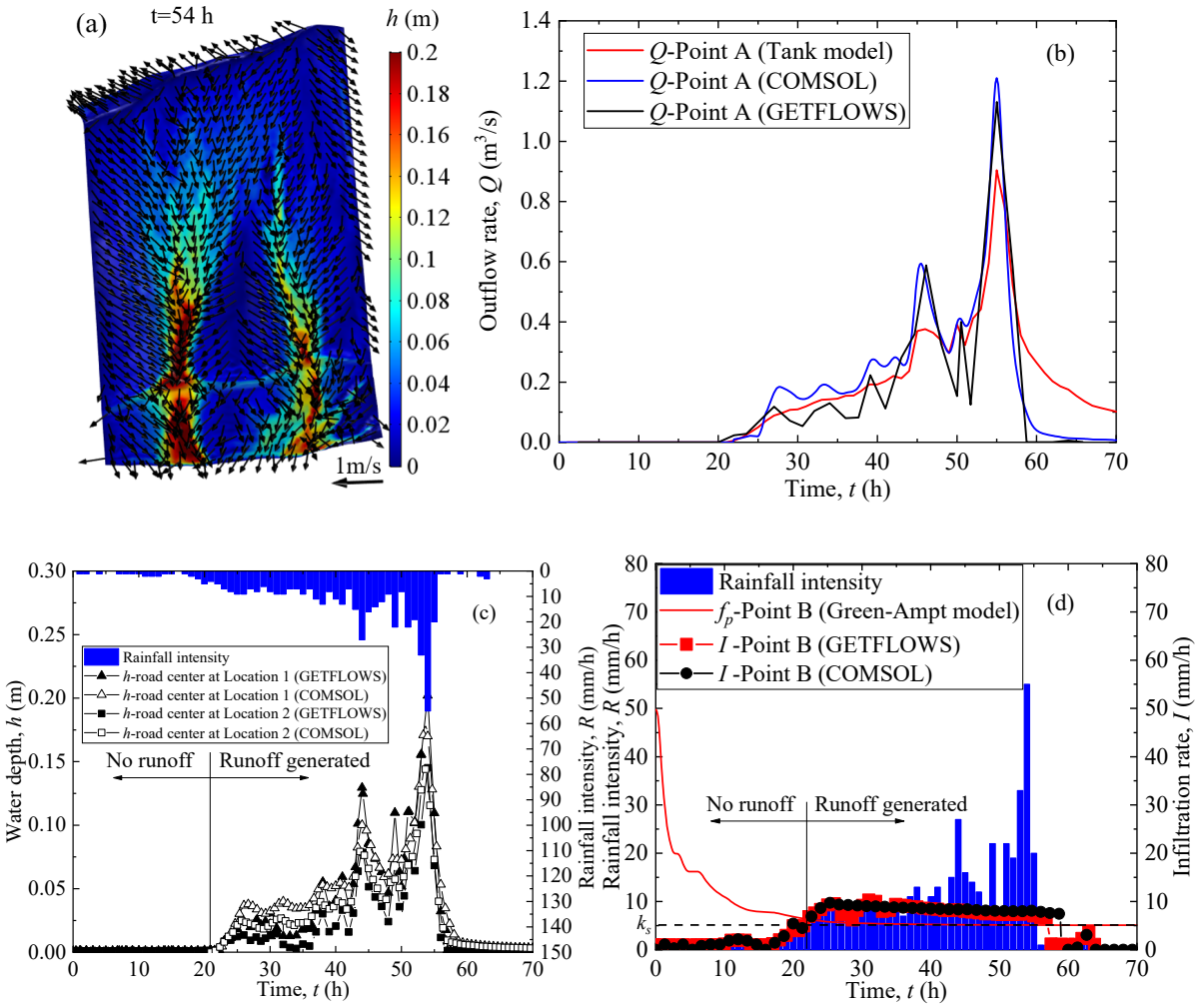

Fig. 8. (a) Distribution of water depth and the vector of flow velocity calculated by COMSOL; (b) Comparison of outflow rate (Q) calculated by each approach; (c) Surface water depth (h) at Location 1 and Location 2; (d) Infiltration capacity (f_p) and infiltration rate (I).

After rainfall intensity exceeds the infiltration capacity (f_p), i.e. the runoff is generated, the infiltration rate is no longer equal to rainfall intensity. At this time, the infiltration rate is governed by the pressure head gradient. The pressure head gradient is controlled by the water depth and the pressure head in the cell below. With the rainwater infiltration, the increase of the pressure head in the cell below is more significant than the increase of the water depth. It means that the pressure head gradient will become smaller compared with when the runoff is

445 just generated, i.e., the infiltration rate decreases with time during runoff as shown in Fig. 8(d).
446 Furthermore, the surface water depth (Fig. 8(c)) and infiltration rate (Fig. 8(d)) calculated by
447 GETFLOWS agree well with the results calculated by COMSOL at both Location 1 and
448 Location 2, meaning that the two software can be mutually verified and the coupled surface
449 and subsurface flows model is more reliable than Tank model.

450 5.3 Slope instabilities assessment along the highway on a small catchment-scale

451 In order to investigate the effect of runoff and subsurface flow on the slope stability
452 during Typhoon No.10, the slope instabilities on a small catchment-scale (including two
453 embankment slopes at Location 1 and Location 2, respectively) are analyzed by using the
454 proposed coupled model. The effects of runoff on the infiltration and subsurface flow are
455 considered by the coupled surface and subsurface flows model proposed in chapter 2. By
456 incorporating the body load (volumetric water content) and pore water pressure (u_w) calculated
457 by the coupled surface and subsurface flows model into the soil mechanics model, two cases
458 are studied, i.e., slope instabilities analysis with considering runoff and without. Fig. 9 shows
459 the distribution of the local factor of safety (F_{LFS}) in the two cases. From Fig. 9(b), it is
460 recognized that with considering runoff, the safe area and two dangerous spots are identified
461 in a 550m wide and 850m long area during the heavy rainfall, i.e., the slope failure occurred
462 ($F_{LFS} < 1.0$) at Location 1 and Location 2 are successfully reproduced. Conversely, without
463 considering runoff, slope failure only occurred in a very small area at Location 1 as shown in
464 Fig. 9(a). Fig. 10 shows the distributed pore water pressure (u_w) and local factor of safety (F_{LFS})
465 at Location 1 and Location 2 under the two study cases (with considering runoff and without).
466 From Fig. 10, it can be seen that the presence of runoff leads to a more significant increase in
467 pore water pressure. The negative pore water pressure increases to zero or even becomes
468 positive pore water pressure in the surface layer of the soil, which causes the occurrence of the

469 slope failure. From Fig. 10(b), it can be seen that the simulated slip surface (red line in Fig.
470 10(b)) is slightly shallower than the actual slip surface (blue line in Fig. 10(b)) at Location 2.
471 The main reason why the simulated slip surface is slightly shallower than the actual slip surface
472 is that in the actual process of slope failure, the collapsed part moved downstream, and runoff
473 further eroded the newly exposed soil and caused further damage of the embankment.
474 Therefore, it implies that runoff has significant effects on the embankment slope failures
475 especially at the exit of the gully. On the other hand, by using the LFS approach, slope
476 instabilities analysis can be performed on a small catchment-scale, which has significant
477 advantages as compared with other methods to analyze the stability of a single slope. Moreover,
478 the distribution map of FOS conduces to determine the dangerous spots in the target area. This
479 has significant implications for precisely determining the dangerous spots (instead of areas) on
480 a small catchment-scale and accurately releasing warning information to the dangerous spots.
481 For example, in Japan, the disaster warning information is released to a 5 km×5 km area
482 according to the national early warning system. Based on the early warning system, the
483 occurrence time of slope failures can be roughly estimated, while it is difficult to determine the
484 specific number and location of slope failures. Therefore, the coupled model of surface flow,
485 subsurface flow, and soil mechanics proposed in this study provides an effective way for
486 simulating heavy rainfall-induced runoff and slope instabilities in the target area. By expanding
487 the size of the coupled model proposed in this paper to 5 km×5 km, the occurrence of slope
488 failures can be roughly predicted by the Japan early warning system, and the dangerous spots
489 can be identified in this wide area by the numerical results. It means that combining the
490 numerical simulation results with the prediction results of an early warning system, warning
491 information will be accurately released to the dangerous spots instead of broader areas.

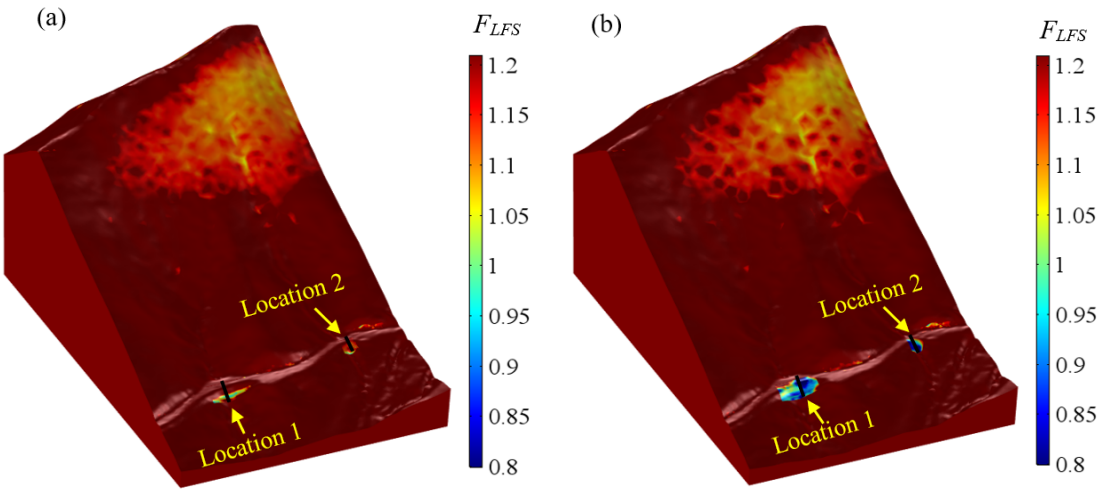

Fig. 9. Distribution map of FOS on the small catchment-scale during Typhoon No.10. (a) Without considering runoff; (b) With considering runoff.

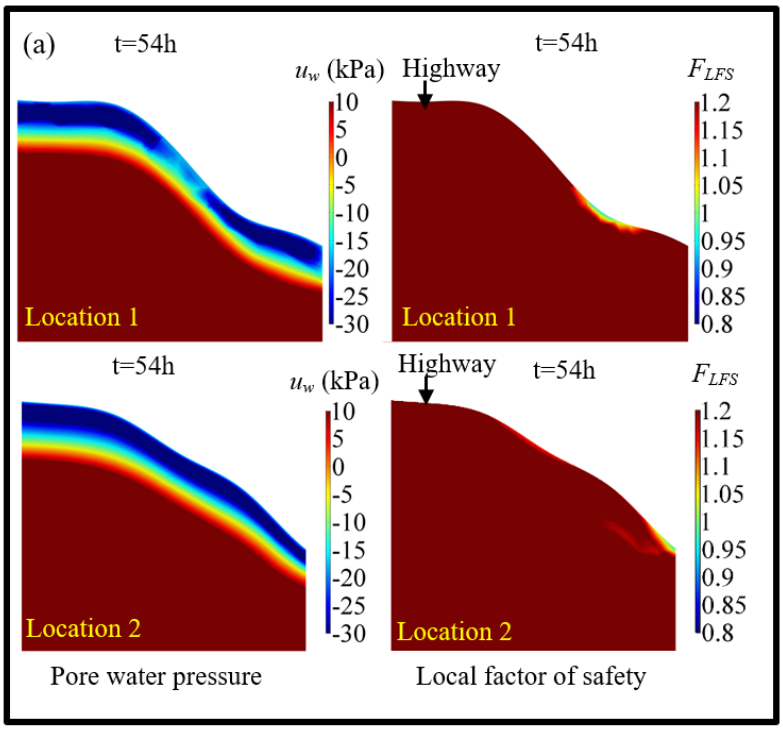

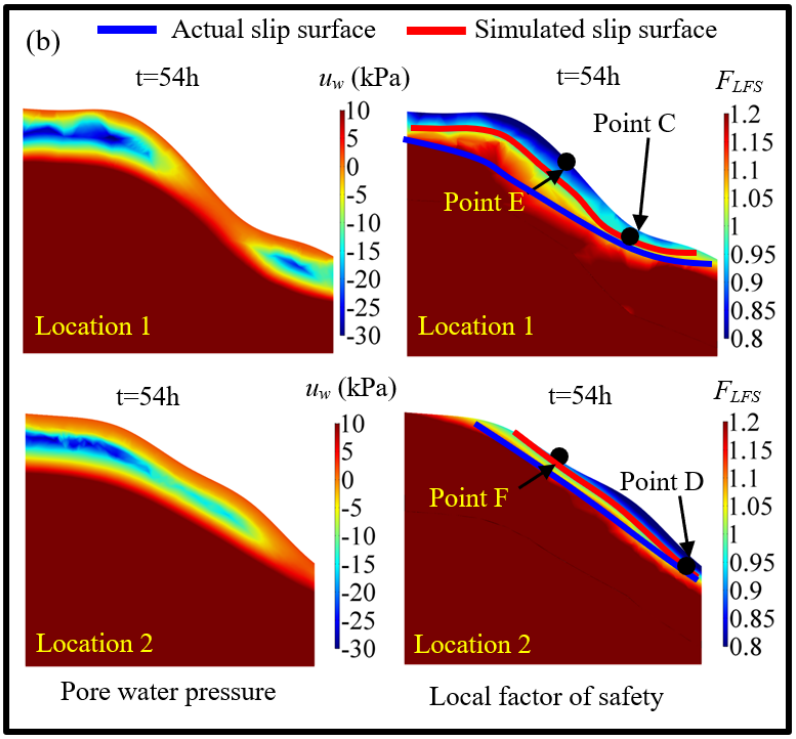

Fig. 10. Distribution of pore water pressure (u_w) and local factor of safety (F_{LFS}). (a) Without considering runoff; (b) With considering runoff.

To further analyze the effect of runoff on slope stability, Fig. 11(a) to Fig. 11(c) illustrates the time-dependent effective degree of saturation (S_e), u_w, and F_{LFS} at Location 1 and Location 2 (Point C and Point D in Fig. 10, located near the ultimate slip surface as shown by the red lines in Fig. 10(b)). It is recognized that the infiltrated rainwater causes the increase of the S_e as shown in Fig. 11(a), which causes an increase in the u_w as shown in Fig. 11(b), thereby causing a decrease in the suction of unsaturated soil, and eventually decreases the F_{LFS} as shown in Fig. 11(c). It is worth noting that the increase of S_e and u_w, and the decrease of F_{LFS} are more significant when the runoff is considered. After runoff is generated, S_e and u_w have a steep increase and F_{LFS} sharp declines, meaning that the runoff from upstream allows more water to infiltrate into the embankment, thereby causing a more significant decrease in the suction of the embankment and the possibility of embankment slope failure at the exit of the gully to be much greater than other locations along the highway. On the other hand, the excessive high-

velocity runoff could allow more water to infiltrate into the embankment and eventually trigger slope failure. Therefore, the runoff is a key factor causing the embankment slope failures, and its effects cannot be neglected. Erosion might occur on the slope surface when the flow velocity exceeds a critical value, called critical erosional velocity, V_c (Blais and McGinn, 2011). The critical erosional velocity is 0.55m/s at Location 1 and Location 2, which is calculated by the critical erosion velocity estimation model (V_c=0.33$D_{50}^{0.47}$) proposed by Bogardi (1978). V_c is critical erosion velocity measured in m/s. D_{50} represents the median diameter of the sediment material in mm, and its value is 3.0 mm for the embankment at Nissho Pass (Kawamura and Miura, 2018). To discuss the effects of the runoff on the erosion of the embankment slope surface, Fig. 11(d) shows the flow velocity (V) on the embankment slope at Location 1 and Location 2 (Point E and Point F in Fig. 9, located on the embankment slope surface). In Fig. 11(d), it can be identified that the flow velocity exceeds the critical erosion velocity, V_c (0.55 m/s), and even close to 1.0 m/s at peak both at Location 1 and Location 2. Therefore, it can be considered as the excessive high-velocity runoff and could cause severe erosion of the embankment slope. Moreover, from Fig. 11(c) and Fig. 11(d), it is recognized that the F_{LFS} becomes less than 1.0 and the flow velocity exceeds V_c at 00:00 on August 31st, 2016 after the road was closed from 11:15 on August 30th, 2016 (the yellow period in Fig. 11(c) and Fig. 11(d)). It means that the simulation results are reliable. However, the runoff induced erosion of the embankment slope is not considered in the numerical simulation of this study. The discussion in the effects of runoff on the erosion of the embankment slope surface and the influences of the erosion on the slope instability is a future assignment in this study.

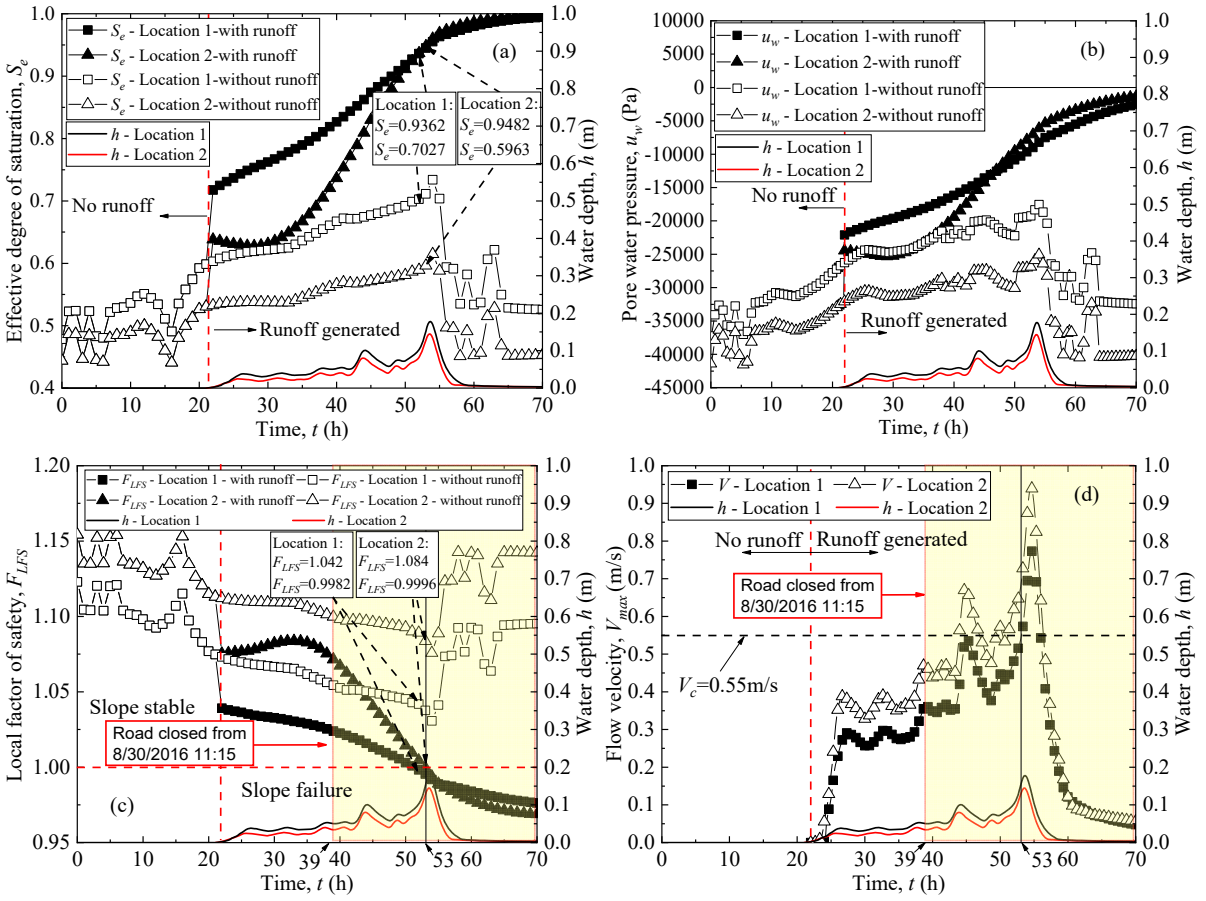

Fig. 11. Time-dependent effective degree of saturation (S_e), pore water pressure (u_w), local factor of safety (F_{LFS}), and flow velocity (V) at Location 1 and Location 2. (a) S_e vs. time; (b) u_w vs. time; (c) F_{LFS} vs. time; (d) V vs. time.

6 Discussions and Conclusions

This study attempts to propose a numerical model that is applicable for simulating heavy rainfall induced runoff and slope instabilities on a small catchment-scale to determine the danger points (instead of areas) in the target area and accurately release warning information. At present, full shallow water equations are mainly used to simulate erosion and flooding. Due to the long calculation time of full shallow water equations, it cannot quickly obtain the calculation result and be applied to practice. Therefore, this study firstly simplified the shallow water equations by ignoring the insignificant terms in the equations of motion. Afterward, as

545 the general commercial software used for stability analysis of slopes can hardly simulate runoff,
546 for example, GeoStudio and FLAC^{3D}. Ignoring runoff is still the main calculation assumptions
547 of surface hydrology in these software. Therefore, this study proposes a coupled model of
548 surface flow, subsurface flow, and soil mechanics, which provides an effective way for
549 simulating heavy rainfall-induced runoff and slope instabilities on a small catchment-scale. In
550 addition, combining the numerical simulation results of the coupled model proposed in this
551 paper with the prediction results of the Japanese early warning system in the target area (e.g. 5
552 km×5 km), warning information will be accurately released to the dangerous spots instead of
553 areas. The findings from this study can be outlined as follows:

554 1. In the equations of motion of shallow water equations, the driving force term and friction
555 term are the main contribution terms, while the total contribution of the inertia term, advection
556 term, and velocity term is less than 1% together. Therefore, the diffusion wave approximation
557 that simplifies the equations of motion by considering only the driving force term and friction
558 term is applicable to the practical runoff analysis.

559 2. The coupled model of surface flow, subsurface flow, and soil mechanics proposed in this
560 study can reflect the two-stage process of rainwater infiltration, i.e. rainfall infiltration in the
561 early stage of rainfall event and runoff infiltration in the later stage of the rainfall event, and it
562 is also applicable to simulate runoff, infiltration, seepage, and slope instabilities on a small
563 catchment-scale.

564 3. Excessive high-velocity runoff is a key factor causing the embankment slope failures at the
565 exit of the gully, and its effects cannot be neglected. In this study, runoff and slope stability
566 with two watersheds (each including an embankment slope) are successfully simulated by the
567 coupled model of surface flow, subsurface flow, and soil mechanics proposed in this study.

The effects of runoff on the slope stability are successfully taken into consideration and the slope failures caused by runoff are reproduced through numerical simulation.

4. The LFS approach is more efficient to predict the rainfall-induced slope failures in the target area by simulating slope instabilities on a small catchment-scale, which has significant advantages as compared with other methods to analyze the stability of a single slope. Furthermore, the distribution map of FOS on the small catchment-scale conduces to determine the dangerous spots in the target area.

The research findings of this study are expected to help improve the numerical model of heavy rainfall-induced surface flow and slope failure, and benefit the prediction of the occurrence of heavy rainfall-induced disasters in the future. Expanding the coupled model proposed in this study to a larger area with more watersheds and combining the numerical results with the prediction results of the Japanese early warning system, as well as the discussion in the effects of runoff on the erosion of the embankment slope surface and the influences of the erosion on the slope instability are future assignments in this study.

Acknowledgments

This study was supported in part by Grants-in-Aid for Scientific Research (A) (16H02360) from the Japan Society for the Promotion of Science (JSPS) KAKENHI. The authors gratefully acknowledge the Hokkaido Regional Development Bureau and Hokkaido Road Management Engineering Center for their surveyed data and comments.

Data Availability

Weather station data and terrain information used in this research are publicly available at the website of Japan Meteorological Agency (http://www.data.jma.go.jp/gmd/risk/obsdl/index.php) and Geospatial Information Authority of Japan (https://www.gsi.go.jp/top.html). The results

591 data obtained in this research are available at the website
592 (https://data.mendeley.com/datasets/2n9zyyyfyz/1).

593 **References**

594 Abdul, A. S., Gillham, R. W., 1984. Laboratory studies of the effects of the capillary fringe on
595 streamflow generation. Water Resources Research. 20 (6), 691-698. doi:
596 10.1029/WR020i006p00691

597 Acharya, G., Cochrane, T. A., Davies, T., Bowman, E., 2009. The influence of shallow
598 landslides on sediment supply: a flume-based investigation using sandy soil. Engineering
599 Geology. 109(3-4): 161-169. doi.org/10.1016/j.enggeo.2009.06.008

600 Bishop, A. W., 1954. The use of pore water coefficients in practice, Géotechnique. 4, 148-152.
601 doi:10.1680/geot.1954.4.4.148

602 Bishop, A. W., 1955. The use of slip circle in the stability analysis of slopes. Géotechnique.
603 5(1), 7-17. doi:10.1680/geot.1955.5.1.7

604 Blais, E. L., McGinn, R. A., 2011. Critical erosion velocity for natural shale gravels: an
605 empirical study. Prairie Perspectives: Geographical Essays. 14, 51-59.

606 Bogardi, J., 1978. Sediment Transport in Alluvial Streams (No. 04; TC175. 2, B6.). Budapest:
607 Akademiai Kiado, 826 p.

608 Chiu, Y. Y., Chen, H. E., Yeh, K. C., 2019. Investigation of the influence of rainfall runoff on
609 shallow landslides in unsaturated soil using a mathematical model. Water, 11(6), 1178.
610 doi: 10.3390/w11061178

611 Chowdhury, R., Flentje, P., 2002. Uncertainties in rainfall-induced landslide hazard. Quarterly
612 Journal of Engineering Geology and Hydrogeology. 35(1), 61-70. doi:
613 10.1144/qjegh.35.1.61

614 COMSOL Multiphysics, 2018. version 5.4, COMSOL Inc., Sweden.

615 Cuomo, S., Della Sala., M., 2013. Rainfall-induced infiltration, runoff and failure in steep
616 unsaturated shallow soil deposits. Engineering Geology. 162, 118-127.
617 doi.org/10.1016/j.enggeo.2013.05.010
618 Farshidfar, N., Nayeri, A., 2015. Slope Stability Analysis by Shear Strength Reduction Method.
619 Journal of Civil Engineering and Urbanism. 5(1), 35-37.
620 Fernández-Pato, J., Caviedes-Voullième, D., Garcia-Navarro, P., 2016. Rainfall/runoff
621 simulation with 2D full shallow water equations: Sensitivity analysis and calibration of
622 infiltration parameters. Journal of Hydrology. 536, 496-513.
623 doi:10.1016/j.jhydrol.2016.03.021
624 Fujisawa, K., Marcato, G., Nomura, Y., Pasuto, A., 2010. Management of a typhoon-induced
625 landslide in Otomura (Japan). Geomorphology. 124(3-4), 150-156. doi:
626 10.1016/j.geomorph.2010.09.027
627 Furuichi, T., Osanai, N., Hayashi, S., Izumi, N., Kyuka, T., Shiono, Y., Miyazaki, T.,
628 Hayakawa, T., Nagano, N., Matsuoka, N., 2018. Disastrous sediment discharge due to
629 typhoon-induced heavy rainfall over fossil periglacial catchments in western Tokachi,
630 Hokkaido, northern Japan. Landslides. 15, 1645-1655. doi:10.1007/s10346-018-1005-1
631 GEO-SLOPE International (2007), GeoStudio, Calgary, Alberta, Canada.
632 GETFLOWS, 2014. Integrated Water Cycle Simulation System. Geosphere Environmental
633 Technology Corp., Japan.
634 Green, W. H., Ampt, G. A., 1911. Studies on Soil Physics, Part 1, the Flow of Air and Water
635 through Soils. Journal of Agricultural Science. 4(1), 1-24. doi:
636 10.1017/S0021859600001441
637 Hong, N., Hama, T., Kitajima, T., Aqili, S. W., Huang, X., Wei, Q., Kawagoshi, Y., 2015.
638 Simulation of Groundwater Levels Using Tank Model with Consideration of Mixed

639 Hydrological Structure in Kumamoto City. Journal of Water and Environment
640 Technology. 13(4), 313-324. doi: 10.2965/jwet.2015.313
641 Horton, R. E., 1933. The role of infiltration in the hydrological cycle. Eos Trans. AGU. 14,
642 446-460. doi: 10.1029/TR014i001p00446
643 Itasca, 2012. Fast Lagrangian Analysis of Continua in 3 Dimensions (FLAC3D), USA
644 Kawamura, S., Miura, S., 2018. Mechanical behavior of decomposed granite soils in Hokkaido
645 and its evaluation. Japanese Geotechnical Journal. 13(2), 159-170. (in Japanese)
646 Kean, J.W., McCoy, S.W., Tucker, G.E., Staley, D.M., Coe, J.A., 2013. Runoff-generated
647 debris flows: Observations and modeling of surge initiation, magnitude, and frequency. J.
648 Geophys. Res. Earth Surf. 118, 2190-2207. doi: 10.1002/jgrf.20148
649 Kitamura, A., Kurikami, H., Sakuma, K., Malins, A., Okumura, M., Machida, M., Mori, K.,
650 Tada, K., Tawara, Y., Kobayashi, T., Yoshida, T., Tosaka, H., 2016. Redistribution and
651 export of contaminated sediment within eastern Fukushima Prefecture due to typhoon
652 flooding. Earth Surf. Process. Landforms. 41, 1708-1726. doi: 10.1002/esp.3944.
653 Liu, J., Yang, C., Gan, J., Liu, Y., Wei, L., Xie, Q., 2017. Stability analysis of road embankment
654 slope subjected to rainfall considering runoff-unsaturated seepage and unsaturated fluid–
655 solid coupling. International Journal of Civil Engineering. 15(6), 865-876. doi:
656 10.1007/s40999-017-0194-7
657 Lu, N., Şener-Kaya, B., Wayllace, A., Godt, J. W., 2012. Analysis of rainfall-induced slope
658 instability using a field of local factor of safety. Water Resources Research. 48, W09524.
659 doi:10.1029/2012WR011830
660 Malow F.A., Shimada S., Hazart A., 2017. Event-based Rainfall-runoff Simulations using
661 GETFLOWS for Kourtimalei Catchment in Djibouti. International Journal of
662 Environmental and Rural Development. 8 (1), 169-175.

663 Morgenstern, N. R., Price V. E., 1965. The analysis of the stability of general slip surfaces.
664 Géotechnique. 15(1), 79-93. doi: 10.1680/geot.1965.15.1.79
665 Mori, K., Tada, K., Tawara, Y., Ohno, K., Asami, M., Kosaka, K., Tosaka, H., 2015. Integrated
666 watershed modeling for simulation of spatiotemporal redistribution of post-fallout
667 radionuclides: Application in radiocesium fate and transport processes derived from the
668 Fukushima accidents. Environmental Modelling & Software. 72, 126-146. doi:
669 10.1016/j.envsoft.2015.06.012
670 Murillo, J., García-Navarro, P., Burguete, J., Brufau, P., 2007. The influence of source terms
671 on stability, accuracy and conservation in two-dimensional shallow flow simulation using
672 triangular finite volumes. Int. J. Numer. Methods Fluids. 54, 543-590. doi:
673 10.1002/fld.1417
674 Okada, K., 2001. Soil Water Index. Meteorological Society of Japan, 48(5), 59-66. (in Japanese)
675 Osanai, N., Shimizu, T., Kuramoto, K., Kojima, S., Noro, T., 2010. Japanese early-warning for
676 debris flows and slope failures using rainfall indices with Radial Basis Function Network.
677 Landslides. 7, 325-338. doi: 10.1007/s10346-010-0229-5
678 Pasculli, A., Calista, M., Sciarra, N., 2018. Variability of local stress states resulting from the
679 application of Monte Carlo and finite difference methods to the stability study of a
680 selected slope. Engineering Geology. 245, 370-389. doi:10.1016/j.enggeo.2018.09.009
681 Rahardjo, H., Lee, T. T., Leong, E. C., Rezaur, R. B., 2005. Response of a residual soil slope
682 to rainfall. Canadian Geotechnical Journal. 42(2), 340-351. doi.org/10.1139/t04-101
683 Rengers, F. K., McGuire, L. A., Kean, J. W., Staley, D. M., Hobley, D. E. J., 2016. Model
684 simulations of flood and debris flow timing in steep catchments after wildfire. Water
685 Resources Research. 52(8), 6041-6061. doi: 10.1002/2015WR018176
686 Richards, L. A., 1931. Capillary conduction of liquids through porous mediums. Physics. 1(5),
687 318-333. doi: 10.1063/1.1745010

688 Sato, A., Hayashi, T., Hayashi, H., Yamaki, M., 2017. On the geotechnical properties of
689 decomposed granite soil in Hokkaido. 57th Technical Report of Hokkaido Branch of
690 Japanese Geotechnical Society. 145-148. (in Japanese)
691 Sciarra, N., Calista, M., Miccadei, E., Pasculli, A., Piacentini, T., Sciarra, M., 2017.
692 Morphometric analysis, multitemporal geomorphological investigation and numerical
693 modelling of the Montebello sul Sangro Large Landslide (Abruzzo-Central Italy). Italian
694 Journal of Engineering Geology and Environment. 1(1), 117-133.
695 doi:10.4408/IJEGE.2017- 01.S-11
696 SoilVision, 2018. Version, 4.23. SoilVision Systems Ltd. Saskatoon, Saskatchewan, Canada.
697 Sugawara, M., Ozaki, E., Watanabe, I., Katsuyama, Y., 1974. Tank model and its application
698 to Bird Creek, Wollombi Brook, Bikin River, Kitsu River, Sanaga River, and Nam Mune.
699 Research Note of the National Research Center for Disaster Prevention 11, Tsukuba,
700 Japan. 1-64.
701 Tian, D., Liu, D., 2011. A new integrated surface and subsurface flows model and its
702 verification. Applied Mathematical Modelling. 35(7), 3574-3586.
703 doi:10.1016/j.apm.2011.01.035
704 van Asch, T.W.J., Yu, B., Hu, W., 2018. The Development of a 1-D Integrated Hydro-
705 Mechanical Model Based on Flume Tests to Unravel Different Hydrological Triggering
706 Processes of Debris Flows. Water, 10(7), 950. Doi:10.3390/w10070950
707 van Genuchten, M. Th., 1980. A closed-form equation for predicting the hydraulic conductivity
708 of unsaturated soils. Soil Science Society of America Journal. 44(5), 892-898. doi:
709 10.2136/sssaj1980.03615995004400050002x
710 Wang, G., Sassa, K., 2003. Pore-pressure generation and movement of rainfall-induced
711 landslides: effects of grain size and fine-particle content. Engineering Geology. 69(1-2),
712 109-125. doi: 10.1016/S0013-7952(02)00268-5

713 Wei, Z., Shang, Y., Zhao, Y., Pan, P., Jiang, Y. 2017. Rainfall threshold for initiation of
714 channelized debris flows in a small catchment based on in-site measurement. Engineering
715 Geology. 217, 23-34. doi.org/10.1016/j.enggeo.2020.105618
716 Weill, S., Mouche, E., Patin, J., 2009. A generalized Richards equation for surface/subsurface
717 flow modelling. Journal of Hydrology. 366, 9-20. doi: 10.1016/j.jhydrol.2008.12.007
718 Zeng, Y. H., Guymer, I., Spence, K. J., Huai, W. X., 2010. Application of analytical solutions
719 in trapezoidal compound channel flow. River Research and Applications. 28 (1), 53-61.
720 doi: 10.1002/rra.1433
721 Zhang, J., Huang, H. W., Zhang, L. M., Zhu, H. H., Shi, B., 2014. Probabilistic prediction of
722 rainfall-induced slope failure using a mechanics-based model. Engineering Geology. 168,
723 129-140. doi.org/10.1016/j.enggeo.2013.11.005